Confined colloidal bilayers under shear: Steady state and relaxation back to equilibrium

René Messina and Hartmut Löwen
Institut für Theoretische Physik II, Heinrich-Heine-Universität Düsseldorf, Universitätsstrasse 1, D-40225 Düsseldorf, Germany
(Received 24 June 2005; revised manuscript received 17 October 2005; published 18 January 2006)

Crystalline bilayers of charged colloidal suspensions which are confined between two parallel plates and sheared via a relative motion of the two plates are studied by extensive Brownian dynamics computer simulations. The charge-stabilized suspension is modeled by a Yukawa pair potential. The unsheared equilibrium configuration is two crystalline layers with a nested quadratic in-plane structure. For increasing shear rates $\dot{\gamma}$, we find the following steady states: First, up to a threshold of the shear rate, there is a static solid which is elastically sheared. Above the threshold, there are two crystalline layers sliding on top of each other with a registration procedure. Higher shear rates melt the crystalline bilayers and even higher shear rates lead to a reentrant solid stratified in the shear direction. This qualitative scenario is similar to that found in previous bulk simulations. We have then studied the relaxation of the sheared steady state back to equilibrium after an instantaneous cessation of shear and found a nonmonotonic behavior of the typical relaxation time as a function of the shear rate $\dot{\gamma}$. In particular, application of high shear rates accelerates the relaxation back to equilibrium since shear-ordering facilitates the growth of the equilibrium crystal. This mechanism can be used to grow defect-free colloidal crystals from strongly sheared suspensions. Our theoretical predictions can be verified in real-space experiments of strongly confined charged suspensions.

DOI: 10.1103/PhysRevE.73.011405 PACS number(s): 82.70.Dd, 83.10.Mj, 61.20.Ja

I. INTRODUCTION

A fundamental understanding of the different processes governing the relaxation of metastable phases back to equilibrium is critical for many basic questions in condensed matter physics and material science. Also, relaxational processes are omnipresent in industrial applications. Colloidal suspensions represent excellent model systems where such questions can be studied directly in real space as the length scales are conveniently accessed experimentally, the (variable) interactions can be described theoretically in a simple way, and the microscopic processes are rather slow as compared to molecular materials. This has been extensively exploited in previous studies of interaction-dependent equilibrium properties and dynamics [1–4]. One important example for a nonequilibrium steady state is a *sheared* colloidal suspension. It is known that application of shear may destroy the underlying equilibrium crystalline structure of the unsheared suspension [5] and can also lead to a reentrance ordering for high shear rates [6]. After cessation of shear the system will relax back to equilibrium from the sheared steady state. The microscopic details of this relaxation process are far from being resolved.

If an additional confinement between two parallel plates is considered [7], various experiments [8–14] reveal a rich and subtle influence of shear on the structure. Accordingly the relaxation back to equilibrium after cessation of shear is a fascinating but complex process which is a competition between wetting effects near the walls and bulk relaxation. In experiments on strongly confined suspensions, for instance, a complex pathway of the relaxation back to equilibrium was obtained [15]: a bilayer bcc crystal was shear-molten to recrystallize as a buckled single-layer triangular lattice which subsequently underwent a martensitic transition back to the equilibrium phase.

Most of the theoretical studies on colloidal suspensions have addressed the influence of linear shear flow on the bulk structure via nonequilibrium Brownian dynamics (NEBD) computer simulations [16] where hydrodynamic interactions [17] are neglected and involve charged colloidal particles modeled by a Yukawa pair interaction [18–27]. Shear-induced melting of colloidal bulk crystals and subsequent reentrant ordering at higher shear rates are confirmed by simulation. More recent works addressing a wall acting on a sheared suspension include a NEBD simulation in a channel [28] and theoretical investigations for a single colloidal particle [29,30].

In the present paper we address the relaxation of shear-induced structures after cessation of shear. We use the standard Yukawa model for confined systems and employ NEBD simulations. Here we focus on the simple and transparent situation of colloidal bilayers which are confined between two parallel plates and sheared via a relative motion of the two plates. The reasons to do so are threefold: First, the equilibrium phase diagram for confined crystalline bilayers interacting via a Yukawa pair potential is known from recent lattice-sum techniques at low temperatures [31]. The phase diagram is drastically influenced by the presence of the walls and differs from its bulk limit. This phase diagram was recently confirmed in experiments on charged suspensions strongly confined between two glass plates [32]. Second, the structure and the defects in a crystalline bilayer are easier to classify than in a multilayer. Last but not least, there are experimental studies for strongly confined situations which are not completely understood and are a challenge for a theoretical treatment [15]. Recent simulation studies of Das and co-workers [33,34] have addressed similar questions regarding sliding bilayers. The model employed in the studies of Das *et al.*, however, is simpler than ours: it does not possess a spatial dimension z perpendicular to the plates and hopping

processes between the layers are ignored. Furthermore, the relaxation back to equilibrium is not investigated in Refs. [33,34].

In order to be specific, we chose the unsheared equilibrium configuration to be two crystalline layers with a nested quadratic in-plane structure. This is the same starting configuration as used in the experiments [15]. For increasing shear rates $\dot{\gamma}$, we find the following scenario of steady states: first, there is a static solid which is elastically sheared until a shear-rate threshold is reached. Then there are two crystalline layers sliding on top of each other with a lock-in registration procedure similar to that observed in recent experiments by Palberg and Biehl [35,36]. Higher shear rates melt the crystalline bilayers and even higher shear rates lead to a reentrant solid stratified in the shear direction. This qualitative scenario is similar to that found in previous bulk simulations [18,20,23]. The shear-induced ordering at high shear rates is reminiscent of the transition towards lane formation in oppositely driven particles [37]. We have then studied the relaxation of the sheared steady state back to equilibrium after an instantaneous cessation of shear and found a nonmonotonic behavior of the typical relaxation time as a function of the shear rate $\dot{\gamma}$. In particular, application of high shear rates accelerates the relaxation back to equilibrium via shear ordering in the steady state. This mechanism can be used to grow defect-free colloidal crystals from strongly sheared suspensions as was proposed by Clark and co-workers [38,39]. Our theoretical predictions can be verified in experiments of confined charged suspensions [15,35,36].

The paper is organized as follows: In Sec. II, we introduce the ground state model for crystalline bilayers. The nonequilibrium Brownian dynamics simulation technique is explained in Sec. III. Results are presented in Sec. IV. Finally we conclude in Sec. V.

II. THE MODEL

In this part, we define our model. This is basically a generalization towards finite temperature of the ground state model used in Ref. [31] concerning the *equilibrium* (i.e., without external applied shear flow) phase diagram of crystalline colloidal bilayers interacting via a Yukawa potential. In detail, our system consists of two layers containing in total N particles in the (x,y) plane. The total area density of the two layers is $\rho=N/A$ with A denoting the layer area in the (x,y) plane. The distance D between the layers in the z direction is prescribed by the external potential confining the system. The particles are interacting via the Yukawa pair potential

$$V_{yuk}^{(part)}(r) = V_0 \frac{\exp(-\kappa r)}{\kappa r}, \tag{1}$$

where r is the center-center separation. The inverse screening length κ which governs the range of the interaction is given in terms of the micro-ion concentration by Debye-Hückel screening theory. The energy amplitude $V_0 = Z^2 \exp(2\kappa R)\kappa/\epsilon(1+\kappa R)^2$ scales with the square of the charges Z of the particles of physical hard core radius R reduced by the dielectric ϵ permittivity of the solvent ($\epsilon=1$ for the dusty plasma). Typically, Z is of the order of 100–100 000 elementary charges such that $V_{yuk}(r)$ at typical interparticle distances can be much larger than the thermal energy k_BT at room temperature, justifying formally zero-temperature calculations. Then the energy scale is set by V_0 alone and phase transitions in large bilayer systems are completely determined by two dimensionless parameters, namely the reduced layer density,

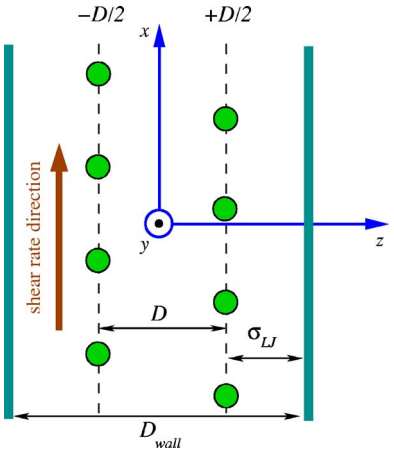

FIG. 1. (Color online) View in the (x,z) plane of the setup of the colloidal bilayer confined between two walls.

$$\eta = \rho D^2/2, \tag{2}$$

and the reduced screening strength,

$$\lambda = \kappa D. \tag{3}$$

For zero temperature, the stable state is solid but different crystalline structures of the bilayers are conceivable. The result for the phase diagram in a (η,λ)-map can be found in Ref. [31]. Here, we explore the same model for finite temperature by computer simulation.

III. THE NONEQUILIBRIUM BROWNIAN DYNAMICS COMPUTER SIMULATION

A. Simulation method

Here, we provide a detailed description of our Brownian dynamics method that was used to investigate *nonequilibrium* sheared colloidal bilayers (at finite temperature). A schematic setup of the system in the (x,z) plane is depicted in Fig. 1. The integration scheme for our model system in the presence of an external steady shear rate $\dot{\gamma}$ reads

$$\mathbf{r}_i(t+\delta t) = \mathbf{r}_i(t) + \frac{D_0}{k_BT}\mathbf{F}_i(t)\delta t + \delta\mathbf{W}_i + \dot{\gamma} z_i(t)\delta t \mathbf{e}_x. \tag{4}$$

Thereby $\mathbf{r}_i(t)=[x_i(t),y_i(t),z_i(t)]$ is the position of the ith colloidal particle at time t and D_0 denotes its free diffusion constant. By imposing a linear velocity profile, the

possibility of solvent shear-banding is excluded. All the contributions to the equation of motion (4) are explained below.

Within a small time interval δt, that particle moves under the influence of the sum of conservative forces $\mathbf{F}_i(t)$ stemming from (i) the pair interaction V_{yuk} [see Eq. (1)] between particle i and the neighboring ones and (ii) the repulsive interaction with the (soft) wall(s) whose potential of interaction, V_{wall}, is modeled as follows:

$$V_{wall}^{(LJ)}(z) = \begin{cases} \alpha\epsilon_{LJ}\left[\left(\dfrac{\sigma_{LJ}}{\dfrac{D_{wall}}{2}-|z|}\right)^{10} - \left(\dfrac{\sigma_{LJ}}{\dfrac{D_{wall}}{2}-|z|}\right)^{4}\right] + \epsilon_{LJ}, & \text{for } \dfrac{\dfrac{D_{wall}}{2}-|z|}{\sigma_{LJ}} \geqslant \left(\dfrac{5}{2}\right)^{1/6}, \\ 0, & \text{for } \dfrac{\dfrac{D_{wall}}{2}-|z|}{\sigma_{LJ}} < \left(\dfrac{5}{2}\right)^{1/6}, \end{cases} \tag{5}$$

where

$$\alpha = -\left[\left(\frac{1}{z_{min}}\right)^{10} - \left(\frac{1}{z_{min}}\right)^{4}\right]^{-1} = 3.070\,02...$$

[with $z_{min}=(5/2)^{1/6}\sigma_{LJ}$ minimizing V_{wall} in Eq. (5)] so that $V_{wall}(\sigma_{LJ})=\epsilon_{LJ}$. This (truncated and shifted) 10–4 Lennard-Jones potential given by Eq. (5) assumes that we have thin soft walls. Note that the use of a 9–3 Lennard-Jones potential corresponding to *semi-infinite* walls would not qualitatively change the results. Also the use of charged hard walls would not affect our main results. To check this latter statement, we have also considered charged walls leading to the following external interaction potential,

$$V_{wall}^{(ch)}(z) = W_0[\cosh(\kappa z) - 1], \tag{6}$$

where the amplitude W_0 is governed by the surface charge density of the plates.

Furthermore, due to the presence of the solvent, the particles experience (i) a friction whose constant is given by k_BT/D_0 and (ii) random displacements, $\delta\mathbf{W}_i$. Those latter are sampled from a Gaussian distribution with zero mean and variance $2D_0\delta t$ (for each Cartesian component). The last term in Eq. (4) represents the applied shear in the x direction and imposes an explicit linear flow field. The zero velocity plane of the imposed shear lies at the midplane between the plates.

B. Parameters

The colloidal particles are confined in a rectangular $L\times L\times D_{wall}$ box where periodic boundary conditions are applied in the (x,y) directions. The system is made up of $N=800$ particles (i.e., 400 particles per layer). The units are set as follows: $k_BT=1/\beta$ sets the energy scale, the (typical average) interlayer separation $D=D_{wall}-2\sigma_{LJ}$ (see also Fig. 1) sets the length scale, and $\tau=D^2/D_0$ sets the time scale. For the screened Coulomb wall-particle interaction [see Eq. (6)] we use $\beta W_0=30$. For the Yukawa interparticle interaction [see Eq. (1)] we choose $\beta V_0=6000$, whereas for the wall-particle interaction [see Eq. (5)] we choose $\beta\epsilon_{LJ}=1$ and $\sigma_{LJ}=0.1D$. The time step was set to $\delta t=10^{-5}\tau$. The reduced colloidal particle density is set to $\eta=ND^2/2L^2=0.24$ (so that $L=40.82D$) and the reduced screening is $\lambda=\kappa D=2.5$. Those latter parameters lead to the staggered square phase in the ground state (or at very low temperature) as can be seen on the phase diagram from Ref. [31].

A time interval of 1.5×10^5 BD time steps (i.e., 1.5τ) was sufficient to obtain the equilibrium (i.e., $\dot\gamma=0$) properties of our model system. The corresponding in-plane (x,y) pair distribution function $g(r)$ is shown in Fig. 2. It clearly shows a high degree of ordering as characterized by the pronounced peaks and the deep minima. The snapshot also provided in Fig. 2 confirms the square lattice structure expected for those parameters. Moreover, the structural properties are insensitive to the kind of particle-wall potential [here Eq. (5) versus Eq. (6)] as expected.

To quantify the layer extension in the z direction we have also plotted the particle density $n(z)$ that can be found in Fig. 3. The mean interlayer separation is then given by $2\int_0^{D_{wall}/2} zn(z)L^2dz \approx 0.99D$, so that (in practice) D corresponds indeed to the interlayer separation. This latter result was identically obtained by employing either Eq. (5) or (6). In the forthcoming, where $\dot\gamma\neq0$, we will only show results for the LJ potential [Eq. (5)]. We have carefully checked that the results are qualitatively the same as those obtained with charged walls [Eq. (6)]. In particular, the general scenario for increasing shear rates does not change.

IV. RESULTS

A. Effect of shear flow

Starting from the equilibrium configuration described in the previous section, an external shear is applied during a

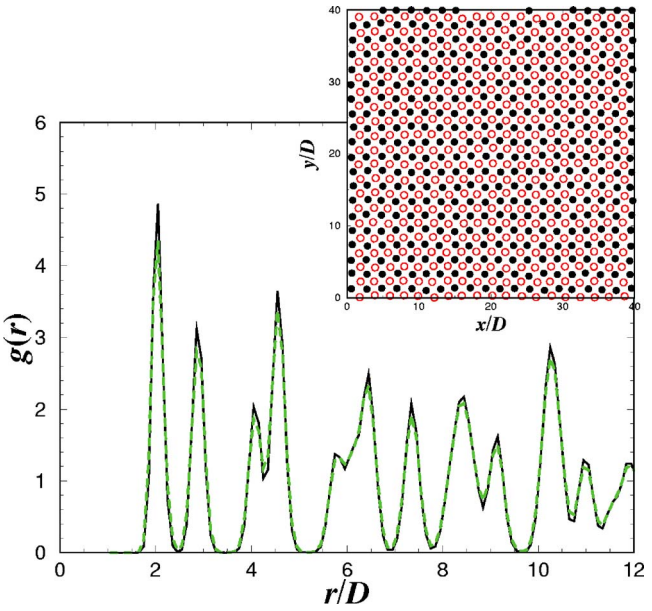

FIG. 2. (Color online) Intralayer (x,y) pair distribution function $g(r=\sqrt{x^2+y^2})$ at equilibrium ($\dot{\gamma}=0$). The solid and dashed lines correspond to the use of Eqs. (5) and (6) (for the wall-particle potential of interaction), respectively. The inset shows a simulation snapshot where the filled (open) circles represent particles belonging to the upper (lower) layer.

period of 4×10^6 BD steps (i.e., 40τ). A steady state is reached after typically 10τ, and subsequent measurements are performed over a typical period of 20τ.

It is instructive to start our study by analyzing the microstructures reported in Fig. 4 corresponding to different $\dot{\gamma}$. From a structural point of view one can (qualitatively) identify three regimes:

• At sufficiently low shear rates (here $\dot{\gamma}=20/\tau$ and $\dot{\gamma}=50/\tau$), it can be seen that the crystalline structure (namely square) as well as the degree of ordering are conserved compared to the equilibrium situation (i.e., $\dot{\gamma}=0$, see Fig. 2). Consequently, we are in an elastic regime.

• For intermediate shear rates (here $\dot{\gamma}=60/\tau$ and $\dot{\gamma}=80/\tau$), there is a (relatively) strong disorder and the structure can therefore be qualified as liquid. In other words we have to deal with a *shear induced melting*.

• At high shear rates (here $\dot{\gamma}=100/\tau$ and $\dot{\gamma}=200/\tau$), the system gets *ordered again* (especially for the highest shear rate $\dot{\gamma}=200/\tau$) but exhibits a different (intralayer) crystalline symmetry (namely a triangular lattice) than the equilibrium one. Consequently, we have a reentrant behavior concerning the *intralayer*-ordering upon shearing.

In order to obtain a more quantitative description of these $\dot{\gamma}$-dependent structural properties, we have also computed the (azimuthally averaged) interlayer- and intralayer-pair-distribution functions $g(r=\sqrt{x^2+y^2})$ for different $\dot{\gamma}$. The results are presented in Fig. 5.

The elastic behavior can be best understood by considering the interlayer and intralayer $g(r)$. From Fig. 5, we see that at weak shearing (here $\dot{\gamma}=20/\tau$), the intralayer crystalline structure as well as the interlayer-lattice-correlation remains unchanged compared to the $\dot{\gamma}=0$ case (the latter is not reported in Fig. 5). At larger shear rate (here $\dot{\gamma}=50/\tau$) the degree of interlayer-lattice-correlation gets weaker than that of the intralayer one. A closer look at Fig. 5(a) reveals that, for $\dot{\gamma}=50/\tau$, the first peak is (asymmetrically) split into two neighboring peaks. This is the signature of a small relative displacement of the two square layer lattices. Upon further increasing the shear rate (now at $\dot{\gamma}=60/\tau$), the bilayer becomes a liquid, demonstrating that there is a critical shear rate $\dot{\gamma}_0$ (below which an elastic behavior is recovered) whose value is such that $50/\tau<\dot{\gamma}_0<60/\tau$.

Above $\dot{\gamma}_0$, the intralayer $g(r)$ exhibits a nontrivial behavior with respect to $\dot{\gamma}$ [see Fig. 5(b)], in agreement with our previous discussion on the microstructures depicted in Fig. 4. More precisely, at intermediate $\dot{\gamma}$ (here $60/\tau$ and $80/\tau$), the intralayer layer structure corresponds to a liquid one. Nonetheless and interestingly, at first neighbor separations, the square structure locally persists, but in coexistence with a triangular structure, as indicated by the broadened (splitted) first peak. This feature can also be nicely visualized on the snapshots from Fig. 4. At high shear rates (here $100/\tau$ and $200/\tau$), there is a strong short-ranged (*re*)ordering into a triangular lattice as indicated by the shifted first pronounced peak (especially for $\dot{\gamma}=200/\tau$). However, the degree of ordering reported for those highly sheared structures is not as high as that observed below $\dot{\gamma}_0$.

In order to quantify the degree of ordering in the x shear direction, we have also investigated the (intralayer) *one-dimensional* pair distribution function $g(|x|)$. For the computation of $g(|x|)$ we consider pairs of particles (of a given layer) that lie within a width $\Delta y/D=0.25$. The results are shown in Fig. 5(c): Below $\dot{\gamma}_0$ and for $\dot{\gamma}=200/\tau$ a crystalline state is found, whereas for the intermediate values of $\dot{\gamma}$ a liquid one is reported. A special case is achieved for $\dot{\gamma}_{max}=100/\tau$ [thick solid line in Figs. 5(b) and 5(c)]: Here there is liquid-like ordering in the shear flow direction [see Fig.

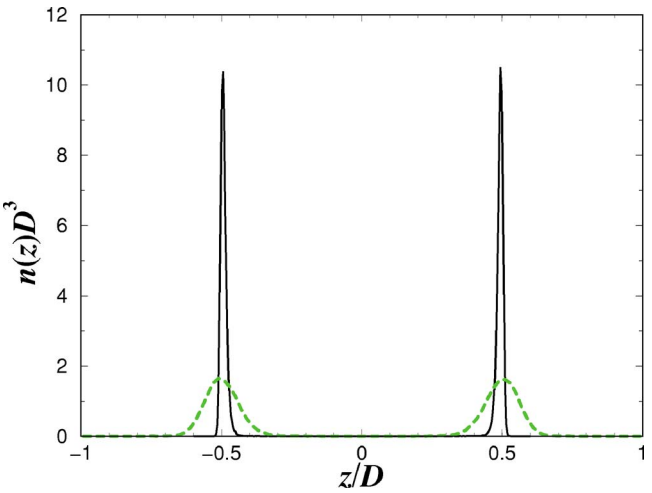

FIG. 3. (Color online) Laterally averaged inhomogeneous particle density $n(z)$ at equilibrium ($\dot{\gamma}=0$). The solid and dashed lines correspond to the use of Eqs. (5) and (6) (for the wall-particle potential of interaction), respectively.

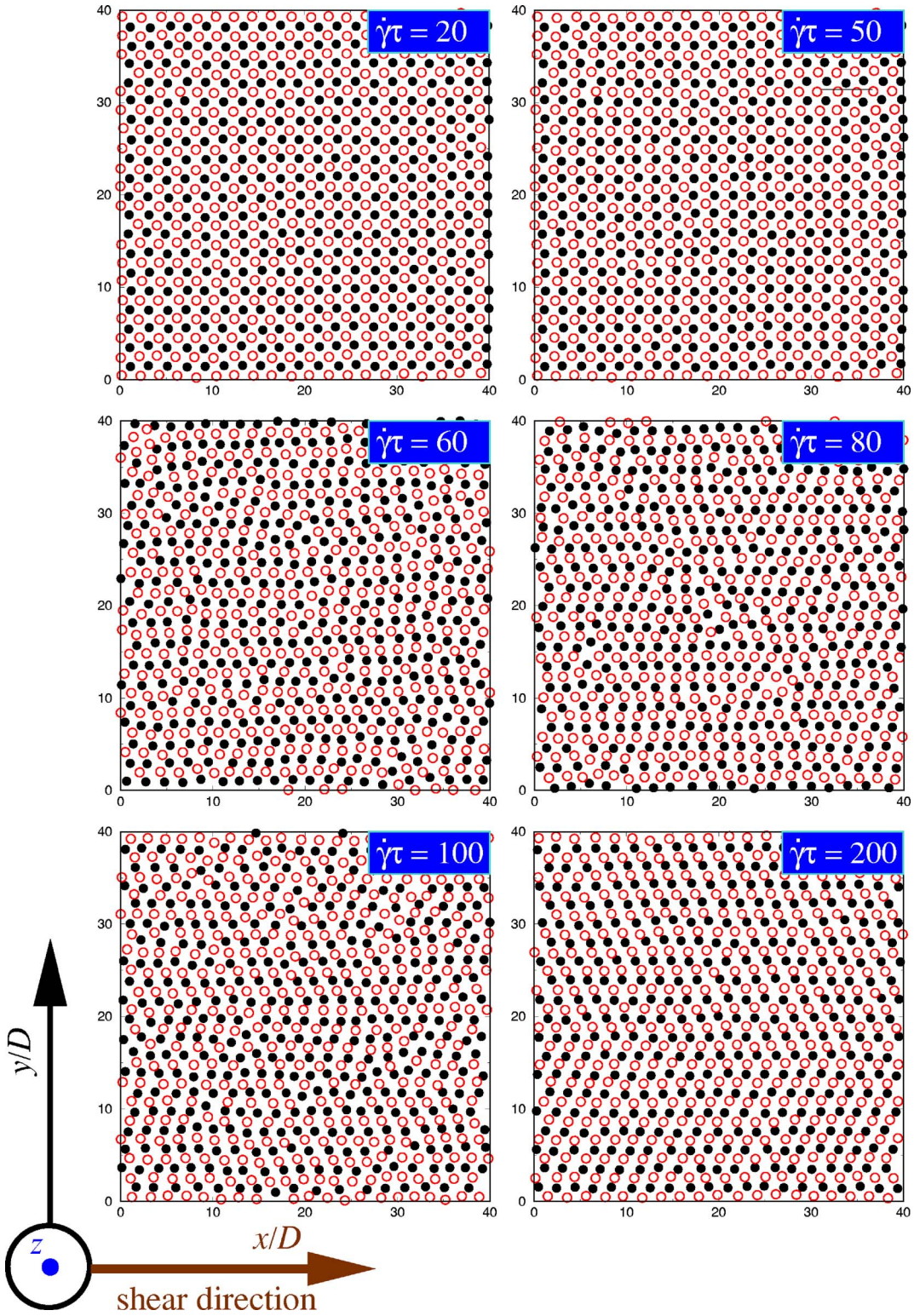

FIG. 4. (Color online) Simulation snapshots for different values of the shear rate $\dot{\gamma}$ (as indicated) where the filled (open) circles represent particles belonging to the upper (lower) layer.

5(c)], but long-ranged solid-like ordering in the radial $g(r)$ [see Fig. 5(b)]. This immediately implies that there is solid-like ordering in the vorticity direction. Hence, this structure can be classified as a liquid crystalline columnar phase.

To further quantify the behavior of highly sheared colloidal bilayers and also to provide a dynamical information, we are going to examine the (dimensionless) modified Lindemann parameter, $\Gamma_L(t)$, that is defined as follows,

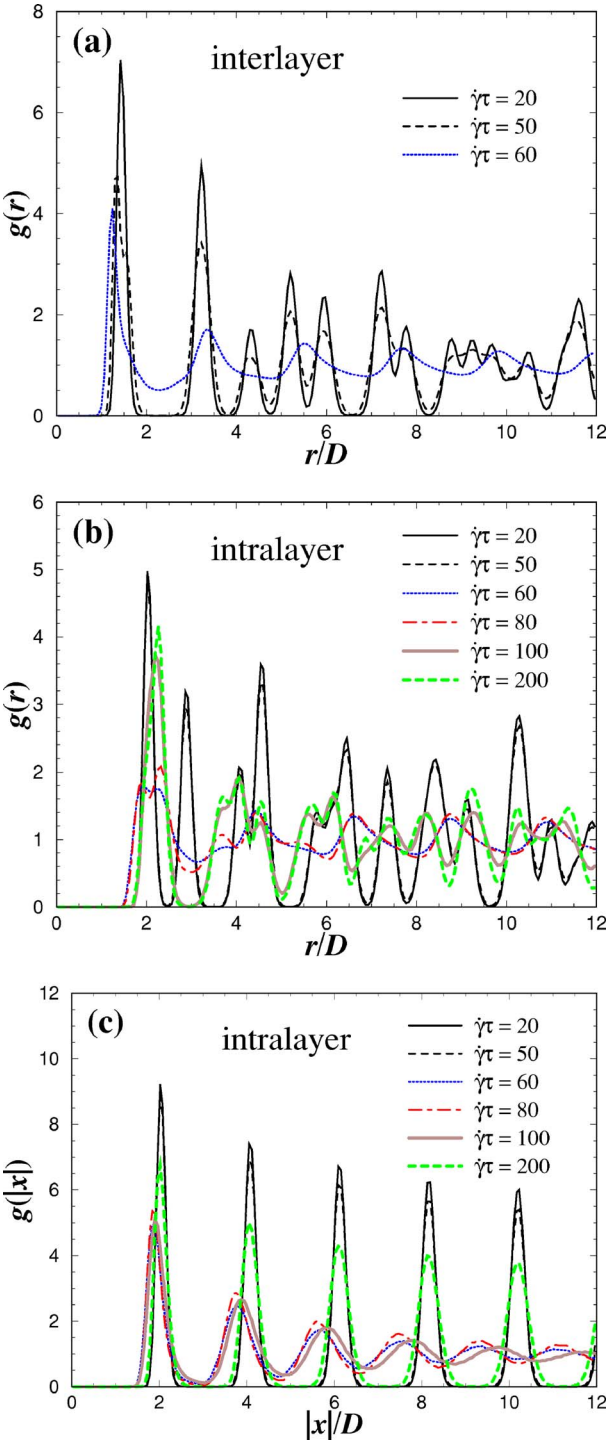

FIG. 5. (Color online) (a) Interlayer (x,y) pair distribution function $g(r=\sqrt{x^2+y^2})$ for small values of $\dot\gamma$ (as indicated in the legend). (b) Intralayer (x,y) pair distribution function $g(r=\sqrt{x^2+y^2})$ and (c) $g(|x|)$ for different values of $\dot\gamma$ (as indicated in the legend). The corresponding simulation snapshots are displayed in Fig. 4.

$$\Gamma_L(t) = \frac{\langle u^2(t)\rangle}{D^2}, \tag{7}$$

where $\langle u^2(t)\rangle$ corresponds to the difference in the mean square displacement of neighboring particles from their initial sites $\mathbf{r}_0=\mathbf{r}(t=t_0)$. More explicitly, $\langle u^2(t)\rangle$ can be written as

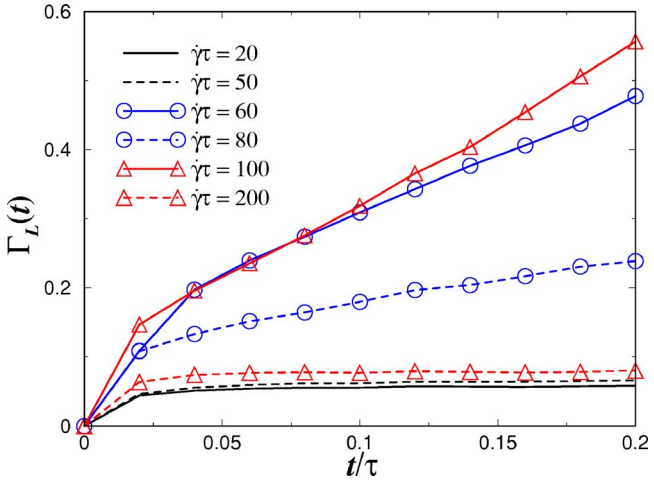

FIG. 6. (Color online) Modified Lindemann parameter $\Gamma_L(t)$ for different values of $\dot\gamma$ (as reported in the legend).

$$\langle u^2(t)\rangle = \left\langle \frac{1}{N}\sum_{i=1}^{N}\frac{1}{N_b}\sum_{j=1}^{N_b}\{[\mathbf{r}_i(t)-\mathbf{r}_i(t_0)]-[\mathbf{r}_j(t)-\mathbf{r}_j(t_0)]\}^2\right\rangle, \tag{8}$$

where $\mathbf{r}_i(t)=[x_i(t),y_i(t)]$, $\langle\cdots\rangle$ denotes an averaging over BD steps and the index j stands for the N_b nearest neighbors of particle i lying in the same upper or lower layers. Typically, for a (local) triangular lattice environment $N_b=6$ while for a rectangular one $N_b=4$. Besides, we also average over several reference times t_0 to improve the statistics. Due to the finite size of the simulation box, one is typically limited to observation times Δt_{obs} of the order of $\Delta t_{obs}\approx L/\dot\gamma_{max}D\approx 0.2\tau$ (by taking here $\dot\gamma_{max}=200/\tau$).

Our results are presented in Fig. 6. In the elastic regime (small $\dot\gamma$), the Lindemann parameter $\Gamma(t)$ exhibits a plateau at

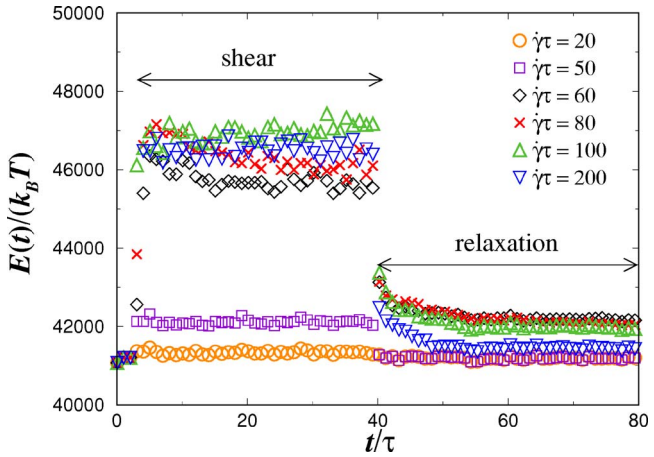

FIG. 7. (Color online) Time evolution of the total potential energy of interaction $E(t)$: before, during, and after shear. The values of $\dot\gamma$, considered during the shear process, are reported in the legend.

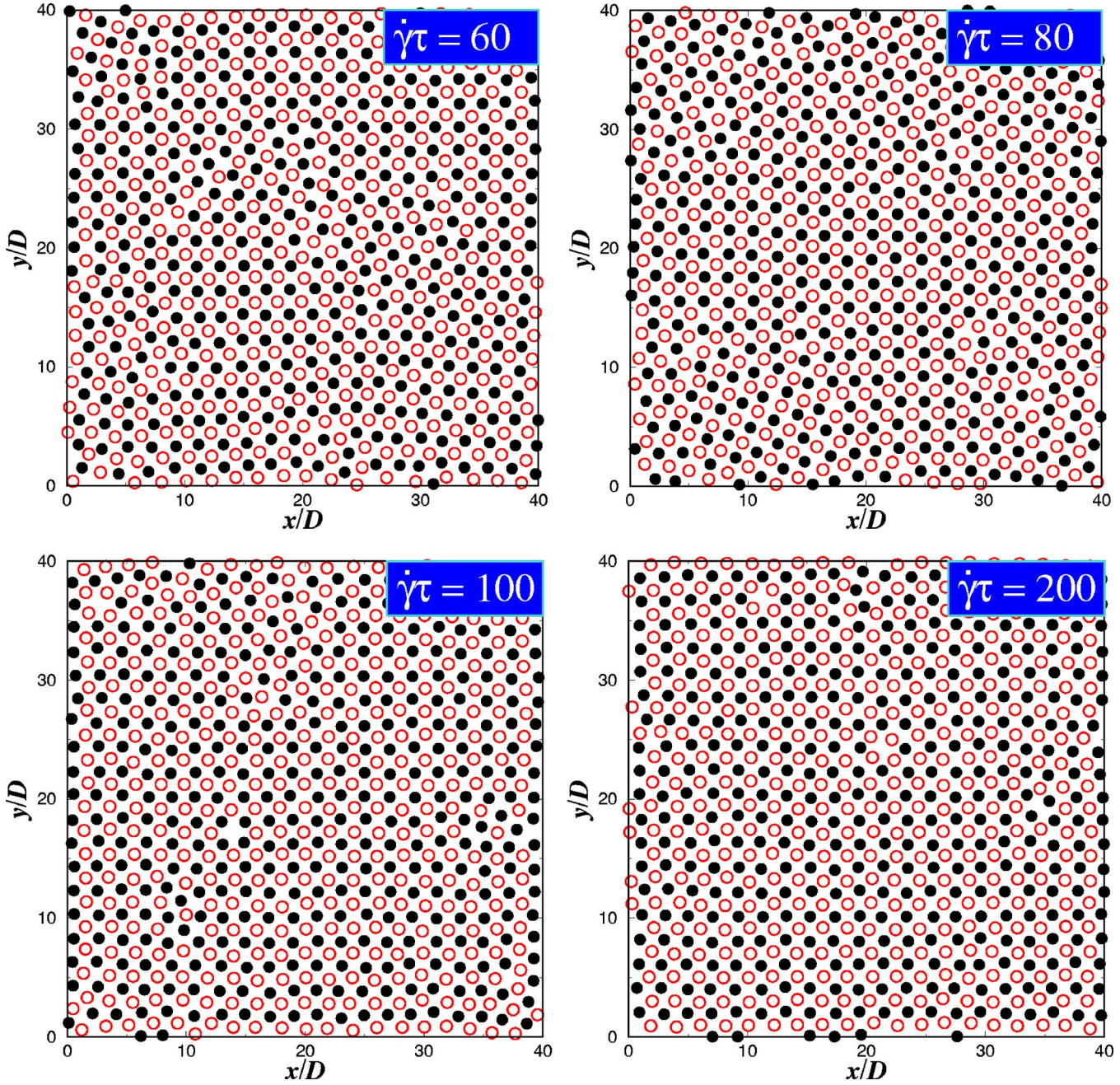

FIG. 8. (Color online) Simulation snapshots of relaxed systems taken at $t=80\tau$ for different values of the prior applied shear rates $\dot{\gamma}$ (as indicated).

"long" times, confirming the crystalline intralayer structure. At higher $\dot{\gamma}$ (i.e., $\dot{\gamma} \geqslant 60/\tau$) the situation gets more complicated. For $60/\tau \leqslant \dot{\gamma} \leqslant 100/\tau$, $\Gamma_L(t)$ diverges, proving a liquid behavior, in agreement with our static analysis of $g(|x|)$ [see Fig. 5(c)]. It is therefore only at very high shear rate (i.e., $\dot{\gamma} \geqslant 200/\tau$) that *true* intralayer crystalline reordering is recovered, as indicated by the existence of the plateau in $\Gamma_L(t)$ whose value is comparable to that obtained in the elastic regime.

B. Relaxation after cessation of shear

We now investigate how the system gets back to equilibrium after cessation of shear. A suitable and simple way to study a relaxation process is to monitor the evolution in time of the total potential energy of interaction $E(t)=V_{yuk}+V_{wall}$. In our simulations, the cessation of shear occurs at $t=40\tau$. Profiles of $E(t)$ for different shear rates $\dot{\gamma}$ applied *prior* relaxation are plotted in Fig. 7. The corresponding microstructures at long time $t=80\tau$ for $60/\tau \leqslant \dot{\gamma} \leqslant 200/\tau$ are sketched in Fig. 8. For low $\dot{\gamma}$ (here $\dot{\gamma} \leqslant 50/\tau$), the relaxation process is very fast as it should be. Note that the equilibrium energy value is not exactly recovered because of the existence of some long-living defects.

The relaxation process gets qualitatively different for more highly sheared systems (here $\dot{\gamma} \geqslant 60/\tau$). For the samples that have undergone a shear-induced melting as de-

duced from our criterion based on $\Gamma_L(t)$ [see Fig. 6 with $\dot{\gamma}\tau=60,80,100$], we remark that they all exhibit a similar relaxation behavior [see Fig. 7 with $\dot{\gamma}\tau=60,80,100$]. In particular the relaxation is thereby much slower, partly due to the existence of *many* long-living defects. Those latter also explain the high energy reported in the long time scale. There are several defects such as dislocations, (low angle) grain boundaries (especially for $\dot{\gamma}\tau=60,80$), and vacancies that are easily identifiable in the snapshots of Fig. 8.

On the other hand, at large enough $\dot{\gamma}$ (here $\dot{\gamma}=200/\tau$), the relaxation is faster as indicated by the faster earlier occurrence of an $E(t)$ plateau (which is also deeper). Nonetheless, the energy of this (nearly) relaxed system remains higher than those that were weakly sheared ($\dot{\gamma}<\dot{\gamma}_0$). Again the existence of some vacancies (see Fig. 8 with $\dot{\gamma}=200/\tau$) increases the energy system as well as the time of *full* relaxation.

By fitting $E(t)$ with an exponential decay, we were able to extract a typical relaxation time, τ_R, for the early stage ($40.5<t/\tau<60$) of the relaxation process: $\tau_R/\tau=5.3(\pm0.1),9.3(\pm0.1),4.7(\pm0.1),4.3(\pm0.1)$ for $\dot{\gamma}\tau=60,80,100,200$, respectively. Those data confirm at least the general trend that very highly sheared samples having strong ordering (prior cessation of shear) relax faster than those moderately sheared having weak ordering.

V. CONCLUSIONS

To conclude we perform Brownian dynamics computer simulations to study crystalline bilayers of charged colloidal suspensions which are confined between two parallel plates and sheared via a relative motion of the two plates. For the parameters under consideration, the unsheared equilibrium configuration is two crystalline layers with a nested quadratic in-plane structure. For increasing shear rates $\dot{\gamma}$, we find the following steady states: first, there is a static solid which is elastically sheared until a shear-rate threshold is reached. Higher shear rates melt the crystalline bilayers and even higher shear rates lead to a reentrant solid stratified in the shear direction. We have then studied the relaxation of the sheared steady state back to equilibrium after an instantaneous cessation of shear and found a nonmonotonic behavior of the typical relaxation time as a function of the shear rate $\dot{\gamma}$. In particular, application of (very) high shear rates accelerates the (post-)relaxation back to equilibrium since shear ordering facilitates the growth of the equilibrium crystal. The steady-state structure may be drastically altered by shearing topographically structured walls (e.g., atomic structures, roughness, chemical patterns, etc.). Hydrodynamic flow effects of the solvent are also expected to have significant influence at high shear rate. These questions will be addressed in future work. We finally point out that similar effects might be present in sheared granular sheets [40].

ACKNOWLEDGMENTS

We thank T. Palberg and C. Wagner for helpful comments. This work was supported by the DFG within the Transregio SFB TR6 (project section D1).

[1] For a review, see P. N. Pusey, in *Liquids, Freezing and the Glass Transition*, edited by J. P. Hansen, D. Levesque, and J. Zinn-Justin (North Holland, Amsterdam, 1991).
[2] W. van Megen, T. C. Mortensen, S. R. Williams, and J. Müller, Phys. Rev. E **58**, 6073 (1998).
[3] H. Löwen, Phys. Rep. **237**, 249 (1994).
[4] H. Löwen, J. Phys.: Condens. Matter **13**, R415 (2001).
[5] B. J. Ackerson and N. A. Clark, Phys. Rev. Lett. **46**, 123 (1981).
[6] B. J. Ackerson and N. A. Clark, Phys. Rev. A **30**, 906 (1984); B. J. Ackerson and P. N. Pusey, Phys. Rev. Lett. **61**, 1033 (1988); B. J. Ackerson, Physica A **174**, 15 (1991); S. E. Paulin, B. J. Ackerson, and M. S. Wolfe, J. Colloid Interface Sci. **178**, 251 (1996).
[7] D. G. Grier and C. A. Murray, J. Chem. Phys. **100**, 9088 (1994).
[8] M. Würth, J. Schwarz, F. Culis, P. Leiderer, and T. Palberg, Phys. Rev. E **52**, 6415 (1995).
[9] A. Heymann *et al.*, J. Colloid Interface Sci. **207**, 119 (1998).
[10] T. Palberg and M. Würth, J. Phys. I **6**, 237 (1996).
[11] M. D. Haw, W. C. K. Poon, and P. N. Pusey, Phys. Rev. E **57**, 6859 (1998).
[12] C. Dux and H. Versmold, Phys. Rev. Lett. **78**, 1811 (1997).
[13] M. R. Maaroufi, A. Stipp, and T. Palberg, Prog. Colloid Polym. Sci. **108**, 83 (1998).
[14] I. Cohen, T. G. Mason, and D. A. Weitz, Phys. Rev. Lett. **93**, 046001 (2004).
[15] J. Weiss, D. W. Oxtoby, D. G. Grier, and C. A. Murray, J. Chem. Phys. **103**, 1180 (1995).
[16] A recent overview about nonequilibrium computer simulations has been given by S. Hess, in *Advances in the Computer Simulation of Liquid Crystals*, edited by P. Parisi and C. Zannoni (Kluwer, Dordrecht, 2000), pp. 189–233.
[17] E. R. Dufresne, T. M. Squires, M. P. Brenner, and D. G. Grier, Phys. Rev. Lett. **85**, 3317 (2000).
[18] W. Xue and G. S. Grest, Phys. Rev. Lett. **64**, 419 (1990).
[19] M. J. Stevens, M. O. Robbins, and J. F. Belak, Phys. Rev. Lett. **66**, 3004 (1991).
[20] M. J. Stevens and M. O. Robbins, Phys. Rev. E **48**, 3778 (1993).
[21] J. Chakrabarti, A. K. Sood, and H. R. Krishnamurthy, Phys. Rev. E **50**, R3326 (1994).
[22] S. Butler and P. Harrowell, J. Chem. Phys. **103**, 4653 (1995).
[23] S. R. Rastogi, N. Wagner, and S. R. Lustig, J. Chem. Phys. **104**, 9234 (1996).
[24] N. Olivi-Tran, R. Botet, and B. Cabane, Phys. Rev. E **57**, 1997 (1998).
[25] S. R. Rastogi, N. Wagner, and S. R. Lustig, J. Chem. Phys. **104**, 9249 (1996).
[26] R. Blaak, S. Auer, D. Frenkel, and H. Löwen, Phys. Rev. Lett.

93, 068303 (2004).
[27] R. Blaak, S. Auer, D. Frenkel, and H. Löwen, J. Phys.: Condens. Matter **16**, S3873 (2004).
[28] M. A. Valdez and O. Manero, J. Colloid Interface Sci. **190**, 81 (1997).
[29] S. G. Bike and D. C. Prieve, J. Colloid Interface Sci. **175**, 422 (1995).
[30] P. Warszynski, X. Wu, and T. G. M. van de Ven, Colloids Surf., A **140**, 183 (1998).
[31] R. Messina and H. Löwen, Phys. Rev. Lett. **91**, 146101 (2003).
[32] A. B. Fontecha, H. J. Schope, H. König, T. Palberg, R. Messina, H. Löwen, 17, S2779 (2005).
[33] M. Das, S. Ramaswamy, and G. Ananthakrishna, Europhys. Lett. **60**, 636 (2002).
[34] M. Das, G. Ananthakrishna, and S. Ramaswamy, Phys. Rev. E **68**, 061402 (2003).
[35] T. Palberg and R. Biehl, Faraday Discuss. **123**, 133 (2003).
[36] R. Biehl and T. Palberg, Europhys. Lett. **66**, 291 (2004).
[37] J. Dzubiella, G. P. Hoffmann, and H. Löwen, Phys. Rev. E **65**, 021402 (2002).
[38] N. A. Clark, A. J. Hurd, and B. J. Ackerson, Nature (London) **281**, 57 (1979).
[39] A. J. Hurd, N. A. Clark, R. C. Mockler, and W. J. Sullivan, Phys. Rev. A **26**, 2869 (1982).
[40] J.-C. Tsai and J. P. Gollub, Phys. Rev. E **70**, 031303 (2004).